In vivo detection and imaging of low-density foreign body with microwave-induced thermoacoustic tomography

Liming Nie, Da Xing,[a)] and Sihua Yang
*MOE Key Laboratory of Laser Life Science, Institute of Laser Life Science, and College of Biophotonics,
South China Normal University, Guangzhou 510631, China*

Radiography or computed tomography is the most widely available imaging tool for foreign body detection. However, the detectability of low-density substances by x ray is very poor when located in soft tissues. Various dielectric loss factors of foreign bodies contribute great microwave absorption heterogeneity compared with the surrounding tissue. A fast thermoacoustic tomography system at 1.2 and 6 GHz was developed to detect foreign targets in small animals. The 6 GHz system had a much higher signal-to-noise ratio in near-surface imaging but smaller imaging depth than the 1.2 GHz system. The effects of microwave distribution inhomogeneity on nonuniform excitation of acoustic pressure were studied and a corresponding calibration algorithm for image distortion was provided and experimentally examined. Thermoacoustic images of radiolucent objects including glass fiber, wood, and bamboo hidden in phantom and residual in living mice were compared with radiography and ultrasonography. Good contrast was obtained between the foreign bodies and the tissue surrounding it, and the location and size of the lesion targets in thermoacoustic images were in good agreement with the actual sample. The experimental results demonstrate that thermoacoustic tomography may become the ideal modality for radiolucent foreign body detection and imaging in animals and human. © *2009 American Association of Physicists in Medicine.*
[DOI: 10.1118/1.3157204]

I. INTRODUCTION

Foreign bodies usually penetrate soft tissues during trauma and iatrogenic cases which include needle, glass, wood, and bamboo. If they are not detected and removed, inflammatory reactions may develop with delayed healing, and possible formation of allergic reaction or acute granuloma or persistent pain may occur.[1–3] Treatment is more likely to work well when the foreign body is found early; hence it is quite important to localize and image the occult object accurately and promptly.

Conventional pulse-echo ultrasound provides structural information corresponding to variations in acoustic impedance. However, ultrasound specificity is limited by the overlapping acoustic features of the foreign body and the surrounding tissue with poor soft tissue contrast.[4] At present, x-ray imaging and computed tomography (CT) are the mass screening tools used most frequently for detecting nonpalpable foreign bodies. However, there are obvious drawbacks of radiography. Repeated x-ray exposure can cause problems to the human body despite using low doses of radiation. Most importantly, they are density dependent and not appropriate for detecting radiolucent substances such as glass fiber and wood. Although magnetic resonance imaging (MRI) is increasingly used as a complementary diagnostic method in medical imaging, study protocols and imaging techniques are not standardized and its spatial resolution is limited. Moreover, MRI is expensive and cumbersome and requires the use of contrast agents which are not innocuous.[5]

Thermoacoustic wave is a result of microwave-induced thermal effect. When irradiated by a short microwave pulse, the tissue is heated up momentarily and acoustic waves are triggered due to thermoelastic expansion. A sample with large dielectric loss factor contrast would absorb microwave strongly, which would lead to acoustic signal with high amplitude. Wide-band ultrasonic transducers are used to acquire the time-resolved acoustic signals. The acquired acoustic signals carry information about the internal thermal and acoustic properties of the tissue. Via image reconstruction, thermoacoustic tomography can be realized based on the heterogeneity in microwave absorption inside the object. Furthermore, extrinsic parameters derived from the dielectric properties provide valuable tissue information associated with certain physiological events.[6] This enables thermoacoustic tomography to serve potentially as functional imaging modalities monitoring physiological processes and differentiating abnormal and normal tissues imperceptible with other imaging methods.

Thermoacoustic imaging offers higher spatial resolution than microwave imaging and allows deeper tissues to be imaged compared with most optical imaging techniques.[7] During the past decade, several research groups have been working on photoacoustic and thermoacoustic imagings of biological tissues.[8–12] Especially breast cancer detection is a promising, focused, and specific application field for thermoacoustic tomography; our group also developed an imaging system at 1.2 GHz for high-contrast breast cancer

imaging.[13–15] Variation of dielectric loss factor is quite significant between normal soft tissues and invaded unknown object. A great difference in dielectric loss factor means high thermoacoustic imaging contrast. Foreign body lesion detection using microwave-induced thermoacoustic tomography, previously uncharted, has become an emerging application by our group.[16] This article greatly extended the previous work mainly in the following areas: (1) Different from the previous simulation using phantoms, current experiments were performed in small animals with improved experimental setup. (2) The rationale for pursuing the detection of foreign objects in soft tissues using thermoacoustic tomography was deduced and clarified by electromagnetic theory. (3) A corresponding calibration algorithm for image distortion was provided to address the nonuniform distribution problem of microwave source. (4) Several different radiolucent substances were tested with an additional microwave frequency at 6 GHz (besides 1.2 GHz) for higher signal-to-noise ratio in near-surface imaging.

II. THEORY

II.A. Thermoacoustic detection of objects with different dielectric loss factors

The complex relative dielectric properties of a tissue can be defined as

$$\varepsilon = \varepsilon_r - j\varepsilon_i, \tag{1}$$

where ε_r is the relative permittivity and the ability of the material to be polarized by the external electric field and ε_i is the dielectric loss factor which quantifies the efficiency with which the microwave energy is converted to heat.

Since $\sigma = \varepsilon_0 \omega \varepsilon_i$, the microwave energy absorption of the radiated tissue is[17]

$$Q(r) = \tfrac{1}{2}\varepsilon_0 \omega \varepsilon_i |E(r)|^2, \tag{2}$$

where ε_0 is the free space permittivity, ω is the microwave frequency, and $E(r)$ is the real electric field inside the tissue. Therefore, the microwave absorption is proportional to the dielectric loss factor of the radiated tissue.

Within the vaporization threshold of the microwave energy employed, the amplitude of the thermoacoustic signal can be approximately written as[18,19]

$$P = \Gamma \cdot \frac{Q(r)}{V}, \tag{3}$$

in which Γ is the Grüneisen parameter [$\Gamma = (\beta c_0^2 / C_p)$, β is the isobaric volume expansion coefficient, c_0 is the speed of ultrasound, and C_p is the specific heat] and V is the unit volume.

Combining Eqs. (2) and (3), we can get

$$P = \Gamma \cdot \frac{1}{2V}\varepsilon_0 \omega \varepsilon_i |E(r)|^2. \tag{4}$$

The Grüneisen parameter is a constant; thus at a certain electric field of the irradiated microwave, the thermoacoustic signal is in linear correlation with the dielectric loss factor. Nor-

mal breast adipose tissue interacts with microwave weakly, while malignant lesion tissue with great dielectric loss factor absorbs microwave strongly, which would lead to high-contrast imaging of breast cancer.[14] Normal biological tissue dominated by polar molecules such as water has a high dielectric loss factor and absorbs microwave strongly, whereas foreign bodies such as glass fiber, wood, and bamboo with much less water content have much lower dielectric loss factors than the surrounding normal tissue. Therefore microwave-induced thermoacoustic tomography based on the differences of their electromagnetic properties has the potential to differentiate and image foreign body lesions. We estimate that the ratio of microwave absorption in the foreign body lesion to the average absorption in the surrounding normal tissue is usually below 0.2. Specifically for fat tissue, the thermoacoustic contrast of foreign body buried in adipose tissue range from 0.3 to 0.5 approximately. That absorption contrast is sufficiently large for the thermoacoustic imaging to differentiate the foreign body lesions clearly.

II.B. Imaging depth at two selectable microwave frequencies

The electromagnetic penetration is infinite in a perfectly transparent substance and zero in reflective material such as metal. Specifically the attenuation coefficient is given by[20]

$$\alpha = \frac{2\pi}{\lambda}\sqrt{\frac{\varepsilon_r(\sqrt{(1+\tan^2 \delta)}-1)}{2}}, \tag{5}$$

in which $\tan(\delta) = \varepsilon_i / \varepsilon_r$.

For a plane wave, incident microwaves decrease to $1/e$ in a penetration distance D_p under the condition $\tan(\delta) \ll 1$, given approximately by

$$D_p = \frac{1}{\alpha} \approx \frac{\lambda}{\pi \tan \delta \sqrt{\varepsilon_r}}. \tag{6}$$

The maximum thermoacoustic imaging depth is affected by the microwave absorption and the noise level. At the frequency employed in our experiments, the penetration depths for fat and muscle at 1.2 GHz are 14 and 2.4 cm, respectively. And for 6 GHz, the penetration depths for fat and muscle are 5.2 and 0.7 cm, respectively.[21] Other soft tissues have a penetration depth between those of muscle and fat. Microwave radiation has a much higher penetration depth than that of photoacoustic imaging and is appropriate for detection of foreign bodies residual in living subjects. The 1.2 GHz system has a much larger image volume than the 6 GHz system due to its lower frequency and larger cross section of the waveguide. On the other hand, the 6 GHz setup has a better signal noise rate (SNR) than the 1.2 GHz in near-surface imaging owing to the larger attenuation of 6 GHz microwaves with the energy transformed to ultrasonic wave in the limited volume. It is appropriate for microwave-induced thermoacoustic tomography to locate and image the deeply hidden foreign objects at two selectable frequencies.
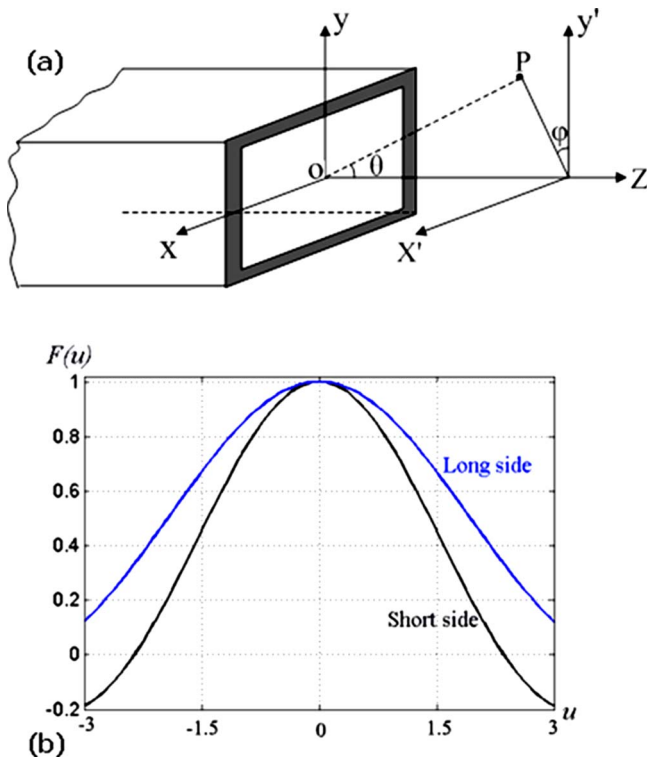
FIG. 1. Schematic illustrations of microwave diffraction in TE_{10} mode. (a) Simulation model of the microwave transmitting out of the aperture surface. (b) Simulated electric field pattern along the two orthogonal directions of the rectangular sides of the waveguide.

II.C. Inhomogeneous distribution of microwave field

The amplitude of the induced thermoacoustic signal is linearly proportional to the irradiated microwave energy currently used according to Eq. (3). Hence the inhomogeneous distribution of the microwave field can be visualized as the cause of microwave-induced sound field nonuniform excitation. Microwave pulse sources at 1.2 GHz (BW-1200HPT, China) and 6 GHz (BW-6000HPT, China) were used in the thermoacoustic tomography experiments. The microwave pulses were coupled into rectangular waveguides in TE_{10} mode with cross sections of 127×63 and 34.8×15.8 mm^2, respectively. Microwave transmitting from the rectangular waveguide to the free space obeys the Huygens diffraction principle; this effect would result in inhomogeneous microwave energy distribution. Take the 6 GHz microwave generator system, for example; both numerical simulation and phantom experiments illustrate this phenomenon. A Cartesian coordinate XYZ was made in the schematic diagram as shown in Fig. 1(a); the center of the aperture surface marked as O, P represents the investigation point in the $X'Y'Z$ plane.

The amplitude function of the electric field along the YOZ plane at point P can be expressed as

$$F_s(\theta) = A \frac{\sin u}{u}. \tag{7}$$

Along the XOZ plane, the amplitude function at point P can be expressed as

$$F_l(\theta) = A \frac{\cos u}{1 - \left(\frac{2}{\pi} u\right)^2}, \tag{8}$$

where $u = \beta l \sin(\theta/2)$, θ is the angle between line OP and axis Z, l is a or b which is the length of the waveguide side, and $\beta = 2\pi/\lambda$ is the phase change along the transmission direction per distance.[22]

The two functions along the two directions are plotted in Fig. 1(b); the upper line marked "Long side" represents the amplitude function F_l along the long side versus u and the lower line marked "Short side" represents the function F_s along the short side. The field intensity changes little away from the center and quickly decreases outside that region. Therefore imaging distortion would be caused especially when the sample is placed at the edge of the microwave radiation.[23] Nevertheless, the imaging distortion depends not only on the field distribution of the microwave source but also on the interaction between the microwave source and the tissue as well as the shape and size of the object. Thus the distortion patterns will not be limited to the diffraction pattern of the microwave source out of the surface aperture discussed in this current work.[24] We provided a partial correction method to alleviate the image distortion caused by the microwave source. However, a complete and new correction method to recover the energy distribution needs more future studies. That is our next step in this work.

II.D. Imaging calibration for thermoacoustic tomography

Via calculating the square of the amplitude functions along the above two orthogonal directions, a two-dimensional (2D) distribution map of the microwave energy out of the aperture surface can be gained. To compensate for the nonuniform distribution of the illumination field, a correction map which was the reciprocal of energy distribution was established to calibrate the thermoacoustic images.

Actually the microwave transmitted out of the waveguide is nonuniform, and our work focused on the field distribution of the microwave illumination source. The microwave illumination source affects the local microwave energy deposition in the tissue. Thus imaging distortion would be caused especially when the sample is placed at the edge of the microwave radiation. Nonuniform excitation of acoustic pressure under inhomogeneous microwave field illumination would lead to a distorted image and strongly nonuniform distributed SNR in the reconstructed image.

Therefore, it is quite necessary to correct the distorted reconstructed images using a calibration map. We derived the microwave field distribution model using Huygens diffraction principle after the electromagnetic wave in TE_{10} mode transmitted out of the waveguide, and then once the calibration map was obtained, the TAT images can be calibrated by dividing the reconstructed image by the calibration map.
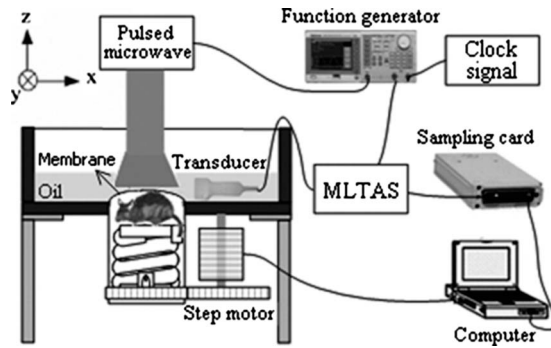
FIG. 2. Schematic diagram of the experimental setup for *in vivo* thermoacoustic tomography system.

III. MATERIALS AND METHODS

III.A. Experimental setup

The hardware system for thermoacoustic tomography is mainly made up of four parts: Microwave irradiating source, signal scanning detector, signal preprocessing system, and data-acquisition (DAS) device. A schematic diagram of the thermoacoustic tomography setup is shown in Fig. 2; two microwave generators at 1.2 and 6 GHz transmitted short microwave pulses adjustable from 0.3 to 1.2 μs; their maximum trigger repetition rates can reach 500 Hz. The energy density per volume of the microwave at 1.2 GHz employed is 0.17 mJ/cm^3, and the energy density for the 6 GHz generator is a little higher at 0.25 mJ/cm^3; these energy dosages are within safety standard for animal and human uses.[25,26] The target or anesthetized mouse to be imaged was placed on a vertical adjustable pad. The tank was filled with transformer oil to couple thermoacoustic waves from the target to the ultrasound detector.

The data-acquisition hardware mainly consists of *B*-mode digital ultrasound diagnostic equipment (model CTS-5000B, Shantou Institute of Ultrasonic Instruments, Shantou, China) with a multielement transducer (L2L50A) and a high speed digital card (PCI-6541, National Instruments, Austin, TX) for collecting digital signals. The digital *B*-mode ultrasound diagnostic equipment with a 320-element transducer was used for detecting and preprocessing thermoacoustic signals. The linear multielement transducer with a scanning width of 53 mm centered at a frequency of 2.5 MHz with a nominal bandwidth of 70%. The signals from the transducer, after preamplification, analog to digital (A/D) conversion with a sampling rate of 25 MHz, and phase adjustment, were acquired with the DAS card and then transferred to the computer for subsequent data processing.

III.B. Signal flow and imaging reconstruction

A beam forming module in the ultrasound system provided a synchronous clock signal as the trigger source. Then the generator function cut down the frequency of the synchronous clock signal to trigger the microwave generator, control its pulse repetition frequency, and synchronize the sampling card. With the multiway electronic switch of the multielement linear transducer array system (MLTAS), the function generator selected several transducer elements of the linear transducer array to capture the induced thermoacoustic signals. The multiway signals are delivered to the dynamic focusing module for phase adjustment and incorporated to one-way signal by delay and sum algorithm, which would improve the SNR.[27–31] After data acquisition of one group of the transducer elements, the next group of elements repeatedly begins to gather signals to form a 2D image. Thermoacoustic and ultrasound images can be obtained simultaneously via switching of the working mode in this *B*-mode digital ultrasound diagnostic equipment.

In this study a transducer array with multielements was used rather than a single transducer; mechanical scanning is no longer compulsory. The data-acquisition time was 5 s for a primary monitoring at one observing stop; multiple view angles were required for a complex network structure. Generally the signals at 20 circular scanning stops around the object were sufficient to recover a clear and accurate image. Due to the directivity properties of the linear transducer array, an improved limited-field-filtered backprojection (LFBP) is employed to reconstruct the thermoacoustic image for boundary information.[32,33] And a modified integration backprojection (mIBP) algorithm using velocity potential is developed to derive inversely the direct microwave absorption distribution of the object.[14]

III.C. *In vitro* biological tissue

Four pieces of pork fatty tissue with arbitrary shapes were sequentially stacked up. A ball of sand, a glass fiber bar, and an iron needle representing targets with different physical densities were embedded under three pieces of pork tissue to testify the ability of x ray for foreign body detection. Also, two pieces of homogeneous pork muscle tissue were cut and made into an arbitrary shape with a thickness of 1 cm. Then a small screwdriver was used to carefully make a straight slot on one piece of pork muscle tissue to place the glass fiber bar. The glass bar was dyed with ink to increase its photographic visibility. Finally, the glass fiber bar was buried beneath another piece of pork muscle tissue for thermoacoustic imaging. The thermoacoustic tomography experiment was conducted with the 6 GHz microwave system.

III.D. Animal mode

BALB/c mice (both genders, 35–45 g body weight) were used in the experiments. General anesthesia was administered to the mice by intraperitoneal injection of pentobarbital (i. p. sodium pentobarbital, 40 mg/kg) to keep the mice motionless through the experiments.[34–36] Before making a model of foreign body retained in living animal, the hair of the object area on the mouse was removed gently with a hair-remover lotion. The mouse was placed on a vertical adjustable pad with a custom-stereotactic mouse holder and then protruded into the tank through an animal hole at the bottom of the tank under a piece of clear membrane. A thin layer of ultrasonic coupling gel was applied on the surface of

the animal body to couple its back and the flexible membrane at the bottom of the water tank. The mice were alive during the whole investigation process.

III.E. Tomographic images at different depths

A thin cylinder ultrasonic lens with a height of 10 mm made from silicon rubber was mounted before the transducer elements. This technical design can produce a geometric focus in front of the transducer array to select 2D image plane and suppress the out-of-plane signals. The computed tomography ability along the vertical direction of the linear transducer array was measured to be about 1.6 mm.[31] Hence vertical slice tomographic images of a foreign body at different depths can be gained. The transducer was fixed on a translation stage for scanning along the vertical direction with a step size of 2 mm. At each depth in the vertical direction, the mouse could be rotated in the horizontal plane for 2D cross imaging. The 1.2 GHz microwave system was employed for lesions at a deeper depth.

III.F. Compared with ultrasound imaging

Ultrasound may miss tiny objects because they have low acoustic contrast or because of operator variability. Also ultrasound specificity is limited by the overlapping acoustic characteristics of foreign bodies and the surrounding tissue. However, thermoacoustic imaging combines the merits of both microwave imaging and ultrasound imaging and achieves excellent microwave absorption contrast and ultrasound spatial resolution.[37,38] A wood strip with a length of 8 mm, which has an acoustic impedance at 1.6×10^6 rayls, almost identical with biological tissue, was found and inserted to a depth of 0.5 cm underneath the lower back of a mouse with an insertion angle of 9° relative to the horizontal plane. After the mouse rehabilitated totally, ultrasonography and thermoacoustic tomography at the frequency of 6 GHz were conducted and compared.

III.G. Compared with x-ray imaging

To validate the applicability of x-ray detection of foreign body *in vivo*, a piece of triangular bamboo with a height of 14 mm and length of 3 mm along the bottom side was vertically inserted to a depth of 1 cm underneath the skin of a mouse abdomen. After the bamboo strip became nonpalpable and total rehabilitation of the mouse, x-ray imaging was conducted with a digital, animal-used x-ray system (piXarray 100 digital specimen radiography systems, Bioptics, Inc., Tucson, AZ). *In vivo* thermoacoustic tomography was carried out using pulsed microwave at 1.2 GHz and compared with the corresponding x-ray image. The mouse was kept alive through the whole experimental process.

IV. RESULTS

A triangle made from iron bar was embedded in agar gel to simulate microwave absorption nonuniformity with the actual phantom shown in the inset of Fig. 3. The shape and size of the triangle in the first reconstructed thermoacoustic
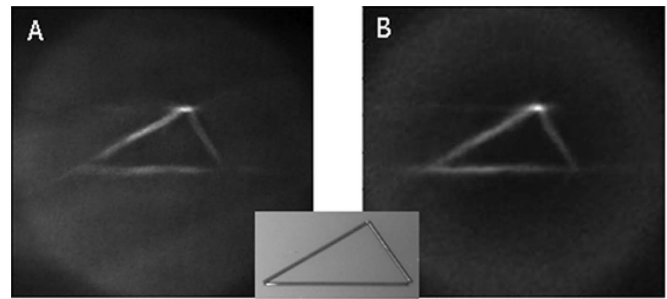

FIG. 3. Thermoacoustic images before and after the calibration. (a) Thermoacoustic image reconstructed from the raw data. (b) The corrected image obtained by dividing (a) by the calculated calibration map.

image [Fig. 3(a)] were easily discernible, but significant distortions appeared. The right angle part placed under the center of the waveguide is the brightest but the two ends on the hypotenuse side had much less magnitudes in value and the two angular points were also obscured. After calibration by dividing Fig. 3(a) by the calculated calibration map, the magnitudes of the angular points at the hypotenuse are increased and more obvious in Fig. 3(b), and the center part keeps unchanged.

Moreover, a phantom made from agar has also been imaged at the 6 GHz microwave setup with and without using the calibration map. The reconstructed thermoacoustic images are shown in Figs. 4(a) and 4(b) with the actual picture of the sample in Fig. 4(d). Great differences exist between the two thermoacoustic results. Without calibration, only the triangular agar close to the scanning center is correctly reconstructed, and the other two triangular agars at the two ends have much less magnitudes in value. The nonuniform pattern is due to the image distortion mechanism discussed in Sec. III. In comparison, Fig. 4(b), after calibration, is clearly imaged and the magnitudes of the two weak images are substantially increased, and the center images keep unchanged. For quantitative analysis of the calibration effect, a white dashed line was selected in the thermoacoustic images as
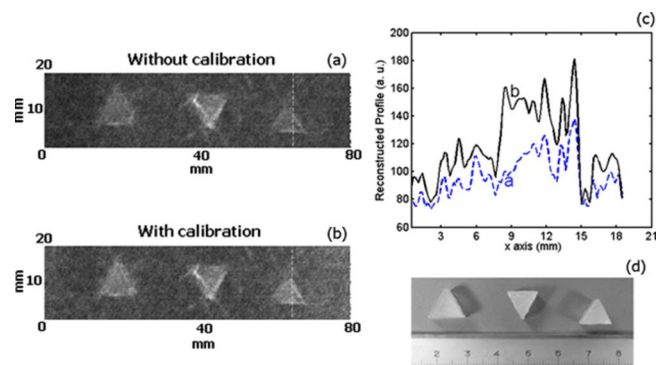

FIG. 4. Three agar gel phantoms and the reconstructed thermoacoustic images. (a) Reconstructed thermoacoustic image of the phantoms without calibration. (b) The corrected image obtained by dividing (a) by the calculated calibration map. (c) The white line profiles of the reconstructed images in (a) and (b) both with $x=4.1$ cm [dashed profile corresponds to (a) and the solid profile corresponds to (b)]. (d) Photography of the three simulated triangular agar.
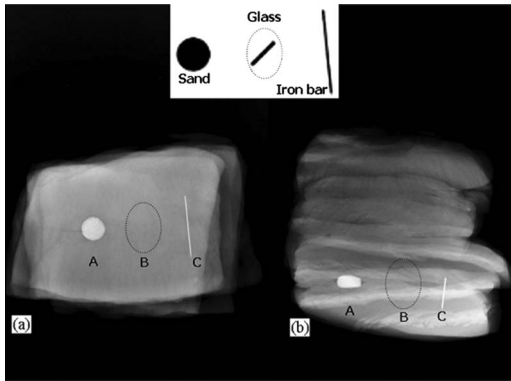
FIG. 5. X-ray imaging of objects with different physical densities. (a) Radiography of sand, glass fiber, and iron bar embedded in biological tissue under the vertical illumination direction. (b) Radiography of the samples embedded in biological tissue under the horizontal illumination direction with the schematic cross section of the samples' placement shown in the inset.

shown in Figs. 4(a) and 4(b) to access the enhanced SNR. The line profiles with the same coordinates corresponding to the lateral axes of the reconstructed images are plotted in Fig. 4(c); the dashed profile marked "a" corresponds to Fig. 4(a), and the solid profile marked "b" corresponds to Fig. 4(b). According to the statistical results, the thermoacoustic contrast can be enhanced two times or more. Also it can be supposed that the farther the distance away from the illumination center, the greater SNR could be enhanced by the calibration. Therefore, the calibration method would achieve an even distribution of SNR and improve the reconstructed image quality.

The x-ray images of the embedded samples with different physical densities along the vertical and horizontal directions are shown in Figs. 5(a) and 5(b), respectively. The sand and the iron needle are easily visible with good agreement with its corresponding schematic as depicted in the inset picture. However, the glass fiber bar is unrecognizable as marked with a dashed circle due to the low physical density of the glass fiber. Hence it is unreliable to use x ray to detect a foreign body of low-density contrast with the surrounding tissue.

The spatial resolution of our thermoacoustic imaging system is estimated to reach 0.5 mm.[14] A phantom of tissue-glass bar was constructed, and the glass fiber bar was dyed with black ink to increase its photographic visibility. The ultrasonic transducer measured the time-of-arrival signals of the thermoacoustic waves. One line signal of the detector received is shown in Fig. 6(a); the first signal peak indicates the tissue boundary and the second peak indicates the glass fiber target. Under microwave illumination with the same energy density, the amplitude of the glass signal is slightly lower than that of the tissue signal. However, as expressed in Sec. III, the field intensity of the microwave changes little away from the center but quickly decreases outside that region; the tissue boundary is exactly outside that region and away from the illumination center. Therefore the microwave energy illuminating the tissue boundary is much lower than
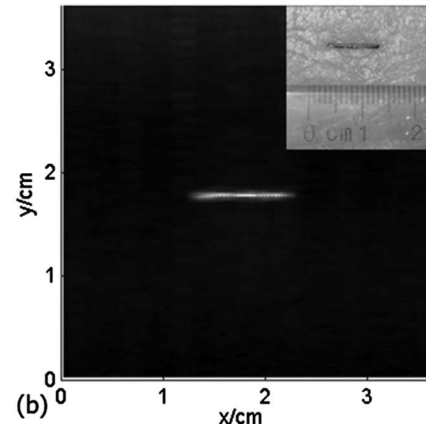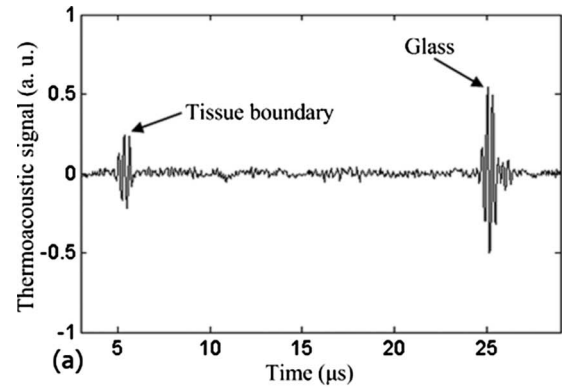

FIG. 6. Thermoacoustic imaging of foreign body with low density. (a) Original acquired thermoacoustic signal of glass fiber strip hidden in pork muscle tissue; the first arrow indicates the tissue boundary and the second one indicates the target. (b) Thermoacoustic image of glass fiber strip hidden in pork muscle tissue.

that illuminating the glass bar, and the amplitude of the glass signal is much higher than that of the tissue signal. From Fig. 6(a), the foreign body to background contrast was estimated to be about 7:1, which demonstrates the imaging contrast advantage of thermoacoustic imaging over x-ray imaging. Also the distances between the thermoacoustic sources and the transducer could be calculated by multiplying the time of arrival with the speed of sound in the medium. The reconstructed thermoacoustic image of the phantom with the glass fiber bar hidden between two pieces of biological tissue is visualized in Fig. 6(b), with the inset showing the actual picture of the sample. The thermoacoustic image recovered by signals at one scanning stop agrees well with the actual phantom. The signals marked "glass" and "Tissue boundary" in Fig. 6(a) were stored in the raw data. In the imaging reconstruction processing, the imaging area was preset; the received thermoacoustic signals were backprojected to that area. Since the imaging area is limited, the signals marked glass are in that area while the tissue boundary signals marked glass are outside that area.

The thermoacoustic and ultrasound images in Fig. 7 indicate the same area of the wood strip in the mouse; the pulse-echo ultrasound image in Fig. 7(b) illustrates the mouse anatomy in the vertical plane (*X-Y* plane), and the skin is visible in the ultrasound images with some obscure organ
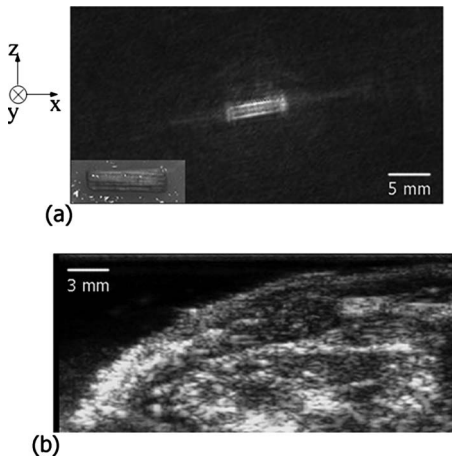
(a)

(b)

FIG. 7. Comparison between *in vivo* thermoacoustic imaging and ultrasonography of wood in living mice. (a) Thermoacoustic image of wood strip residual retained underneath the skin with the actual sample shown in the inset. (b) Ultrasound image of the mouse back; the skin is visible in the ultrasound images, but the wood is indiscernible.
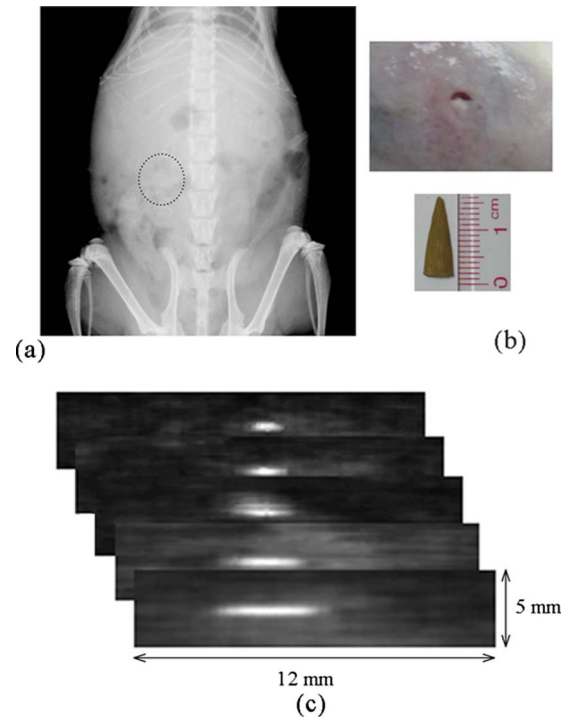

(a)

(b)

(c)

FIG. 8. Comparison between *in vivo* thermoacoustic imaging and x-ray imaging of bamboo strip residual in living mice. (a) X-ray imaging of the living mouse with the bamboo hidden in the body as marked in the dashed circle. (b) Photographs of the inserted traumatic area of the mouse and the bamboo strip, respectively. (c) Five thermoacoustic images along the vertical direction of the bamboo strip.

edges. However, the wood strip is indiscernible due to its similar ultrasound impedance with the biological tissue. The thermoacoustic image in Fig. 7(a) revealed the object contrast in the living mouse in the horizontal plane (*X-Z* plane). It can be seen that the location and size of the wood strip can be distinctly imaged with high spatial resolution [the sample is shown in the inset of Fig. 7(a)].

Images acquired from two microwave sources with different frequencies were compared; the 1.2 GHz system has a much larger imaging depth but a lower SNR than the 6 GHz system in near-surface imaging. As can be seen from Fig. 7(a), obtained on the 6 GHz system, and Fig. 8(c), on the 1.2 GHz system, for near-surface imaging the 6 GHz setup has a better SNR than the 1.2 GHz system due to the larger attenuation of 6 GHz microwaves and the higher-power density of the microwave source. Image registration can be done by combining the reconstructed thermoacoustic images with traditional ultrasound image or x-ray image. With good image registration, the foreign body information obtained with radiography can also be used with thermoacoustic tomography for long term monitoring. These imaging registration technologies would efficiently enhance diagnostic performance.[39,40]

A piece of bamboo retained in living mouse was imaged. Figure 8(b) shows the photography of the inserted traumatic area of the mouse and the bamboo strip, respectively. The reconstructed thermoacoustic images of the bamboo strip, which consisted of five slices, are depicted in Fig. 8(c). Figure 8(a) is the x-ray image of the mouse with the residual bamboo strip. The morphology of the body outline, the spine, and rib bones are well illustrated whereas the foreign body to be detected is totally unrecognizable as marked by the dashed circle in Fig. 8(a). The thermoacoustic image sequence was acquired by moving the scanning head with a step of 2 mm along the vertical direction away from the top of the bamboo piece at one observing angle. It can be seen that the cross section of the object can be imaged with high

contrast and spatial resolution. The length of the bamboo piece in the cross-sectional image increases with the depth. At the same time, the endogenous signal background level rises with lower image SNR due to microwave energy attenuation in deep tissues.

V. CONCLUSION AND DISCUSSION

In our study, imaging of foreign body lesions was carried out using *in vitro* samples and living small animals as a precursor to actual patient study. Rotating the multielement linear transducer array at several scanning stops can capture multiple image signals to yield a cross-sectional image with comprehensive tissue information. At one observing stop, however, the initial structural and function status of the test object can be monitored by the detector array. In our experiments, the multielement linear transducer array employed could acquire one slice image without any rotation.[27,29,31] Furthermore, adopting several multielement transducer arrays spaced around the rotation center with the same angle and same distance, mechanical rotation of the transducer is no longer needed. Therefore, application of thermoacoustic tomography for foreign body detection on human anatomy is also viable and could be realized. A correction method to alleviate the thermoacoustic imaging distortion was provided based on the theoretical analysis and the reconstructed images were compensated for properly. More correction algorithms are needed to recover the real object morphology

from the distorted image. The dielectric loss factor of the invaded foreign body is quite different from that of the normal biological tissue, which would result in great microwave absorption contrast enhancement between the two subjects. More information about the foreign body can be gathered using multiple frequency microwave stimulation; the location and size of the targets in thermoacoustic images were in good agreement with the actual samples at the current two selectable frequencies. Also, the thermoacoustic images can be complemented by alternative imaging approaches for more anatomical and functional information.

The amount of traumatic hemorrhage depends on the lesion position injured; if big vessels were not encountered, hemorrhage is very limited. In our experiments, the foreign bodies are inserted carefully into the muscle tissue, and the thermoacoustic imaging experiments were done after the foreign bodies became nonpalpable and the rehabilitation of the mouse. At the same time, blood has similar microwave absorption as muscle tissue; for example, the dielectric loss factors of blood and muscle are 20.03 and 19.52, respectively, at 6 GHz. Moreover, the hematoma induced by the invaded foreign bodies in the tissue almost disappeared after several-day rehabilitation. The inflammation mainly comprised of macrophage foam cells, free lipids, and collagen and may also be accompanied by angiogenesis and hemorrhage. Compared with the great microwave absorption contrast between foreign body and the normal tissue, the contrast of microwave absorption between inflammatory substances and normal tissue is almost negligible. Therefore, the influence of blood and inflammation to thermoacoustic tomography is quite minimal. In the reconstruction process, we assumed a uniform ultrasound speed in the tissue sample without considering a change in the ultrasound speed in the lesion region. Actually, the ultrasound speed in the foreign body lesion is a little faster than the counterpart speed in the normal tissue. This may partly explain why the size of the lesion measured from the TAT image was smaller than the size measured from the photograph, but it was not expected to be noticeable. Also, impedance differences between the embedded object and normal tissue would result in acoustic wave reflection, thus imaging artifacts. These influences are minimal. Further work that explicitly considers the difference in ultrasound speed between lesions and the surrounding tissue can potentially improve the accuracy of this method.

The plane of our detector array scanning trajectory is vertical to the microwave illumination plane. The detector array employed in the experiments has a computed tomography capability; it selects the thermoacoustic signals which are parallel to its center cross section in a limited view.[33] Hence limited specific orientations of the proposed material can be gained; that is a limitation of our current data-acquisition geometry. Our future work will focus on data acquisition of reflection mode different from the current vertical mode; via volume imaging reconstruction three-dimensional imaging could be realized, and then a 2D image from any observing orientation to the applicator could be extracted from the 3D image, although the *in vivo* thermoacoustic images obtained with this prototype should improve as the technology matures. The thermoacoustic tomography system is a very promising imaging configuration and can be featured by acquisition rapidness and recovery accuracy. Microwave can reach deep objects hidden in the tissue due to its long wavelength. In comparison with x-ray imaging and ultrasound imaging, the thermoacoustic tomography can fill the blind zone for the x-ray band and may become an ideal and low cost modality for radiolucent foreign body detection and imaging in human and animals.

ACKNOWLEDGMENTS

[a]Author to whom correspondence should be addressed. Electronic mail: xingda@scnu.edu.cn; Telephone: +86-20-8521-0089; Fax: +86-20-8521-6052.

[1]R. Blankenship and T. Baker, "Imaging modalities in wounds and superficial skin infections," Emerg. Med. Clin. North Am. **25**(1), 223–234 (2007).

[2]M. Orlinsky *et al.*, "The comparative accuracy of radiolucent foreign body detection using ultrasonography," Am. J. Emerg. Med. **18**(4), 401–403 (2000).

[3]D. W. Kaylor *et al.*, "The utility of bedside ultrasound for the detection of soft tissue foreign bodies in the emergency department," Ann. Emerg. Med. **46**(3), S79–S79 (2005).

[4]C. D. Lehman *et al.*, "Cancer yield of mammography, MR, and US in high-risk women: Prospective multi-institution breast cancer screening study," Radiology **244**(2), 381–388 (2007).

[5]C. Kuhl, "The current status of breast MR imaging—Part I. Choice of technique, image interpretation, diagnostic accuracy, and transfer to clinical practice," Radiology **244**(2), 356–378 (2007).

[6]M. Lazebnik *et al.*, "A large-scale study of the ultrawideband microwave dielectric properties of normal, benign and malignant breast tissues obtained from cancer surgeries," Phys. Med. Biol. **52**, 6093–6115 (2007).

[7]R. A. Kruger, D. R. Reinecke, and G. A. Kruger, "Thermoacoustic computed tomography-technical considerations," Med. Phys. **26**, 1832–1837 (1999).

[8]H. F. Zhang, K. Maslov, G. Stoica, and L. V. Wang, "Functional photoacoustic microscopy for high-resolution and noninvasive in vivo imaging," Nat. Biotechnol. **24**, 848–851 (2006).

[9]M. Eghtedari *et al.*, "High sensitivity of in vivo detection of gold nanorods using a laser optoacoustic imaging system," Nano Lett. **7**(7), 1914–1918 (2007).

[10]R. A. Kruger, K. K. Kopecky, A. M. Aisen, D. R. Reinecke, G. A. Kruger, and W. L. Kiser, "Thermoacoustic CT with radio waves: A medical imaging paradigm," Radiology **211**, 275–278 (1999).

[11]A. De La Zerda *et al.*, "Carbon nanotubes as photoacoustic molecular imaging agents in living mice," Nat. Nanotechnol. **3**, 557–562 (2008).

[12]X. Jin, Ch. Li, and L. V. Wang, "Effects of acoustic heterogeneities on transcranial brain imaging with microwave-induced thermoacoustic tomography," Med. Phys. **35**(7), 3205–3214 (2008).

[13]R. A. Kruger, K. D. Miller, H. E. Reynolds, W. L. Kiser, D. R. Reinecke, and G. A. Kruger, "Breast cancer in vivo contrast enhancement with thermoacoustic CT at 434 MHz—Feasibility study," Radiology **216**, 279–283 (2000).

[14]L. Nie *et al.*, "Microwave-induced thermoacoustic scanning CT for high-contrast and noninvasive breast cancer imaging," Med. Phys. **35**(9), 4026–4032 (2008).

[15]M. Pramanik, G. Ku, C. Li, and L. V. Wang, "Design and evaluation of a novel breast cancer detection system combining both thermoacoustic

(TA) and photoacoustic (TA) tomography," Med. Phys. **35**(6), 2218–2223 (2008).

[16] L. Nie, D. Xing, D. W. Yang, L. M. Zeng, and Q. Zhou, "Detection of foreign body using fast thermoacoustic tomography with a multielement linear transducer array," Appl. Phys. Lett. **90**, 174109–174111 (2007).

[17] B. Guo, J. Li, H. Zmuda, and M. Sheplak, "Multifrequency microwave-induced thermal acoustic imaging for breast cancer detection," IEEE Trans. Biomed. Eng. **54**(11), 2000–2010 (2007).

[18] H. K. Park, D. Kim, and C. P. Grigoropoulos, "Pressure generation and measurement in the rapid vaporization of water on a pulsed-laser-heated surface," J. Appl. Phys. **80**(7), 4072–4081 (1996).

[19] M. W. Sigrist, "Laser generation of acoustic waves in liquids and gases," J. Appl. Phys. **60**(7), R83–R121 (1986).

[20] R. Pelster, "Bounds for local and average microwave absorption in heterogeneous systems," J. Colloid Interface Sci. **318**(2), 534–540 (2008).

[21] C. C. Johnson and A. W. Guy, "Nonionizing electromagnetic wave effects in biological materials and systems," Proc. IEEE **60**, 692–718 (1972).

[22] P. Rattanadecho, "The simulation of microwave heating of wood using a rectangular wave guide: Influence of frequency and sample size," Chem. Eng. Sci. **61**, 4798–4811 (2006).

[23] C. Li, M. Pramanik, G. Ku, and L. V. Wang, "Image distortion in thermoacoustic tomography caused by microwave diffraction," Phys. Rev. E **77**, 031923-1–031923-7 (2008).

[24] K. Yee, "Numerical solution of initial boundary value problems involving maxwell's equations in isotropic media," IEEE Trans. Antennas Propag. **14**, 302–307 (1966).

[25] Y. Xu and L. H. V. Wang, "Rhesus monkey brain imaging through intact skull with thermoacoustic tomography," IEEE Trans. Ultrason. Ferroelectr. Freq. Control **53**, 542–548 (2006).

[26] "IEEE Standard for Safety Levels with Respect to Human Exposure to Radio Frequency Electromagnetic Fields 3 kHz to 300 GHz," IEEE Std C95.1, 2005.

[27] B. Z. Yin, D. Xing, Y. Wang, Y. G. Zeng, Y. Tan, and Q. Chen, "Fast photoacoustic imaging system based on 320-element linear transducer array," Phys. Med. Biol. **49**, 1339–1346 (2004).

[28] L. M. Zeng, D. Xing, H. M. Gu, D. W. Yang, S. H. Yang, and L. Zh. Xiang, "Fast microwave-induced thermoacoustic tomography based on

multi-element phased-controlled focus technique," Chin. Phys. Lett. **23**, 1215–1218 (2006).

[29] Y. Zeng, D. Xing, Y. Wang, B. Yin, and Q. Chen, "Photoacoustic and ultrasonic coimage with a linear transducer array," Opt. Lett. **29**, 1760–1762 (2004).

[30] D. Feng *et al.*, "Microwave-induced thermoacoustic tomography: Reconstruction by synthetic aperture," Med. Phys. **28**(12), 2427–2431 (2001).

[31] C. G. A. Hoelen and F. F. M. de Mul, "Image reconstruction for photoacoustic scanning of tissue structures," Appl. Opt. **39**(31), 5872–5883 (2000).

[32] D. W. Yang, D. Xing, H. M. Gu, Y. Tan, and L. M. Zeng, "Fast multielement phase-controlled photoacoustic imaging based on limited-field-filtered back-projection algorithm," Appl. Phys. Lett. **87**, 194101–194103 (2005).

[33] D. W. Yang, D. Xing, S. H. Yang, and L. Z. Xiang, "Fast full-view photoacoustic imaging by combined scanning with a linear transducer array," Opt. Express **15**, 15566–15575 (2007).

[34] S. Yang, D. Xing, Q. Zhou, L. Xiang, and Y. Lao, "Functional imaging of cerebrovascular activities in small animals using high-resolution photoacoustic tomography," Med. Phys. **34**, 3294–3301 (2007).

[35] Q. Wang *et al.*, "Visualizing localized dynamic changes during epileptic seizure onset in vivo with diffuse optical tomography," Med. Phys. **35**, 216–224 (2008).

[36] Y. Lao *et al.*, "Noninvasive photoacoustic imaging of the developing vasculature during early tumor growth," Phys. Med. Biol. **53**, 4203–4212 (2008).

[37] Z. Q. Zhang, Q. H. Liu, C. Xiao, E. Ward, G. Ybarra, and W. T. Joines, "Microwave breast imaging: 3D forward scattering simulation," IEEE Trans. Biomed. Eng. **50**, 1180–1189 (2003).

[38] A. Fenster, D. B. Downey, and H. N. Cardinal, "Three-dimensional ultrasound imaging," Phys. Med. Biol. **46**, R67–R99 (2001).

[39] B. Zitova and J. Flusser, "Image registration methods: A survey," Image Vis. Comput. **21**(11), 977–1000 (2003).

[40] H. Jiang, Ch. Li, D. Pearlstone, and L. L. Fajardo, "Ultrasound-guided microwave imaging of breast cancer: Tissue phantom and pilot clinical experiments," Med. Phys. **32**(8), 2528–2535 (2005).